# Massive Intracellular Remodeling of CuS Nanomaterials Produces Nontoxic Bioengineered Structures with Preserved Photothermal Potential

Alberto Curcio, Aurore Van de Walle, Emilia Benassai, Aida Serrano, Nathalie Luciani, Nicolas Menguy, Bella B Manshian, Ara Sargsian, Stefaan Soenen, Ana Espinosa, et al.

ACSNANO

www.acsnano.org

ARTICLE

# Massive Intracellular Remodeling of CuS Nanomaterials Produces Nontoxic Bioengineered Structures with Preserved Photothermal Potential

Alberto Curcio, Aurore Van de Walle, Emilia Benassai, Aida Serrano, Nathalie Luciani, Nicolas Menguy, Bella B. Manshian, Ara Sargsian, Stefaan Soenen, Ana Espinosa, Ali Abou-Hassan,* and Claire Wilhelm*

Cite This: https://doi.org/10.1021/acsnano.1c00567

Read Online

ACCESS | Metrics & More | Article Recommendations | Supporting Information

**ABSTRACT:** Despite efforts in producing nanoparticles with tightly controlled designs and specific physicochemical properties, these can undergo massive nano−bio interactions and bioprocessing upon internalization into cells. These transformations can generate adverse biological outcomes and premature loss of functional efficacy. Hence, understanding the intracellular fate of nanoparticles is a necessary prerequisite for their introduction in medicine. Among nanomaterials devoted to theranostics are copper sulfide (CuS), which provides outstanding optical properties along with easy synthesis and low cost. Herein, we performed a long-term multiscale study on the bioprocessing of hollow CuS nanoparticles (CuS NPs) and rattle-like iron oxide nanoflowers@CuS core−shell hybrids (IONF@CuS NPs) when inside stem cells and cancer cells, cultured as spheroids. In the spheroids, both CuS NPs and IONF@CuS NPs are rapidly dismantled into smaller units (day 0 to 3), and hair-like nanostructures are generated (days 9−21). This bioprocessing triggers an adaptation of the cellular metabolism to the internalized metals without impacting cell viability, differentiation, or oxidative stress response. Throughout the remodeling, a loss of IONF-derived magnetism is observed, but, surprisingly, the CuS photothermal potential is preserved, as demonstrated by a full characterization of the photothermal conversion across the bioprocessing process. The maintained photothermal efficiency correlated well with synchrotron X-ray absorption spectroscopy measurements, evidencing a similar chemical phase for Cu but not for Fe over time. These findings evidence that the intracellular bioprocessing of CuS nanoparticles can reshape them into bioengineered nanostructures without reducing the photothermal function and therapeutic potential.

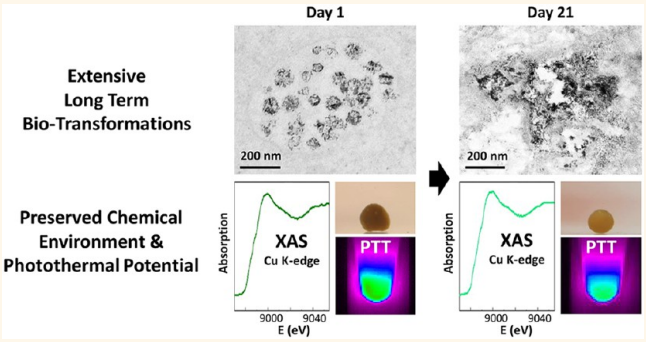


**KEYWORDS:** *biodegradation, biocompatibility, biosynthesis, CuS nanoparticles, magnetic nanoparticles, photothermia*

Inorganic nanohybrids are designed with multiple capabilities, which are tailored for specific therapeutic or diagnostic purpose, and assembled all-in-one. The complex architectures of these nanomaterials imply a coexistence of multiple compositions, a control of size and shape, and a stabilization and functionalization *via* surface coating, altogether to provide original biomedical solutions.[1] Their pursued aptitudes include detection,[2] therapeutic efficiency with synergistic multifunction,[3−7] and safety.[8−10] Importantly, one major issue these engineered nanohybrids have to face is their possible modifications once in the complex biological environment, such as the formation of a protein corona inside blood circulation.[11−14] Moreover, an increasing number of studies demonstrated that inorganic nanoparticles (NPs) can also undergo drastic changes, such as intracellular degradation, upon endocytosis into the endosomal/lysosomal compartments.[15−22] One of the most commonly studied NPs are the magnetic ones, based on an iron oxide core. In this case, the core degradation translates into a loss of the magnetic

Received: January 20, 2021
Accepted: May 12, 2021

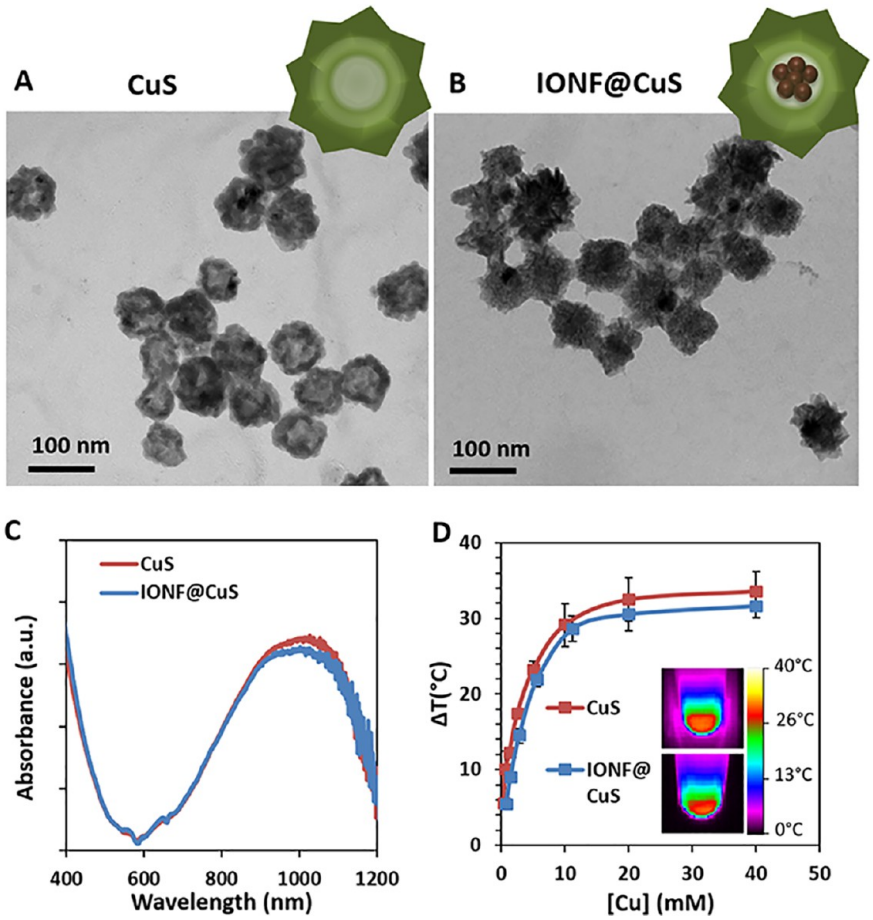


**Figure 1. Copper sulfide nanoassemblies. (A, B) Transmission electron microscopy (TEM) images of hollow substoichiometric $Cu_{2-x}S$ NPs (B) and rattle-like NPs composed of an IONF core bearing a $Cu_{2-x}S$ assembly shell. (C) Absorbance spectra showing a similar near NIR absorption band around 1000 nm. (D) Comparative analysis of the heating of a 10 $\mu$L NP suspension at increasing concentration from [Cu] = 0.1 to 40 mM, upon laser exposure at 1064 nm and 0.3 W $cm^{-2}$ laser power density, for a 5 min duration. Representative infrared (IR) thermographic camera images are shown in the inset for [Cu] = 20 mM.**

properties.[23] The loss of magnetism implies a decreased efficiency for their biomedical applications[24] as imaging and therapeutic agents. Other types of NP composition, such as plasmonic silver, have also been reported to undergo intracellular degradation, leading to a drastic loss of the photothermal therapy (PTT) potential.[25] The magnetic or the silver cores covered with gold[25,26] or polymeric[23,27] shells can then act as a shield against degradation and favor maintenance of magnetic or plasmonic therapeutic functions. Some studies also reported the fate of NP coating *in vivo*, where a clear dismantling of the nanostructures emerged after circulation in the organism.[28,29] Upon biodegradation, the nanoparticle core dissolution induces the release of ions (typically iron or silver), which prompts an adaptation of the cellular metabolism. The released ions were generally stored in the ferritin protein,[25,30] but could also be used for generation of newly biomineralized magnetic nanoparticles.[30,31]

Among the multifunctional NPs that are particularly promising for the biomedical field, those based on copper sulfide (CuS) are emerging as a promising class with numerous therapeutic features.[32−34] Their light-to-heat conversion efficiencies are among the highest,[33,35] and they provide dual laser-mediated treatments for both photothermal and photodynamic therapies in the most preferred second near-infrared biological window,[33,34,36] situated between 1000 and 1700 nm, appealing for its deep penetration, low optical absorption and scattering from biological substrates, and low tissue autofluorescence. One of the peculiar aspects of CuS-based materials resides in the origin of their optical absorption, which is responsible for their photothermal conversion and is still under debate. While some attributed such absorption to plasmonic effects resulting from free hole oscillations in the semiconductor, others assigned it to a valence band transition, independent from the solvent or the surrounding environment, as opposed to plasmonic NPs, but both mainly governed by the chemical composition of NPs.[37,38]

Hollow CuS-based nanostructures have received increasing interest in the field of nanomedicine over the last years. They can be used as cargos for drug delivery applications due to their hollow porous organization and for thermal therapy thanks to their physical plasmonic properties.[39,40] By comparison to other CuS nanoparticles, the sacrificial templating method used for the synthesis of hollow CuS nanostructures is green (water/70 °C) and reproducible and can be easily scaled up to meet biomedical applications. Finally, the same methodology can be transposed for growing hollow copper sulfide shells of the same morphology and composition (core and surface) around any inorganic core, such as one composed of magnetic nanoparticles, what makes them even more attractive. Very recently, we have demonstrated that rattle-like magnetic iron


https://doi.org/10.1021/acsnano.1c00567
ACS Nano XXXX, XXX, XXX−XXX

oxides@CuS nanohybrids are promising theranostic agents.[33] Considering all these advantages, it appears that the biofate and bioprocessing of such nanomaterials inside cells and their impact on their physical theranostic properties should be investigated. To date, few studies have explored the biodegradation of CuS structures. Those were performed *in vivo*[40] or in acidic- and ionic-based environments mimicking the lysosomal content[41] and evidenced the bioinstability of CuS-based nanomaterials. This instability has yet to be explored within living cells.

Here, we propose a tissue model based on human mesenchymal stem cells to explore in depth the long-term intracellular fate of CuS, synthesized as nanoassemblies. This 3D cellular model, organized in a compact spheroid form, allows the quantitative monitoring of NPs' functional activities and structural transformations over almost a month. Hollow CuS nanoassemblies and rattle-like hybrids featuring an iron oxide nanoflower (IONF) core and a CuS shell were investigated. The latter nanostructure allows both the analysis of a combined CuS/iron oxide transformation and also the use of the magnetic core as a tracer of the degradation. Cellular uptake and toxicity screening including reactive oxygen species (ROS) production and impact on stem cell differentiation were conducted upstream. Electron microscopy was employed to observe the intracellular structural evolution of the nanomaterials, highlighting an extensive structural instability. Near infrared photoinduced heating (light-to-heat conversion efficiency) was monitored alongside the biological processing, to provide information on the evolution of the functional potential and thus its time-scale range of applicability. Unexpectedly, almost no loss of photothermal potential was detected over the whole period of analysis (21 days). This observation was confirmed in cancer cell spheroids. Conversely, an almost total loss of magnetism was revealed in the case of the CuS/iron oxide nanohybrids (IONF@CuS). A final proof brought by X-ray absorption spectroscopy (XAS) measurements at the spheroid scale at the Fe and Cu K-edge energies confirmed a strong modification of the iron chemical environment, but no significant change in the copper one. Thus, we demonstrate here an intracellular processing of copper-based nanomaterials featuring both a massive structural transformation and the preservation of its functional physical properties. On a practical level, CuS nanoassemblies position themselves as efficient photoresponsive nanomaterials that retain their function in a biological environment in the long-term and despite their biological processing.

## RESULTS AND DISCUSSION

**Photothermal-Responsive Copper Sulfide Assemblies.** Substoichiometric hollow $Cu_{2-x}S$ nanoassemblies, hereafter named copper sulfide (CuS), and a rattle-like iron oxide nanoflower core surrounded by copper sulfide assemblies (IONF@CuS) were prepared by a two-step water-based template sacrificial synthesis followed by their surface modification with PEG (Figure 1 A and B, respectively), as described in the Materials and Methods section.[33] The CuS and IONF@CuS nanoparticles featured an average diameter of 62 ± 8 nm and 68 ± 9 nm, respectively, measured on transmission electron microscopy (TEM) images. In the case of IONF@CuS, the diameter of the nanoflower-like magnetic core was 24 ± 5 nm (typical TEM image shown in Figure S1). Both nanostructures exhibit a similar hydrodynamic size with an average of about 90 nm, stable in cellular media (DLS, Figure S2), and a similar broad near-infrared (NIR) absorption band centered around 1000 nm (Figure 1C). Their exposure to a 1064 nm laser at low power density (0.3 W/cm$^2$) for 5 min induced a high temperature elevation (Figure 1D), with, for [Cu] over 10 mM, a 30 °C temperature increase $\Delta T$ reached for both nanoassembly formulations. Figure S3 also provides the calculation of the light-to-heat conversion efficiency, with an average value of (42 ± 6)%.

**Internalization and Photothermia in Cells.** Hollow CuS and rattle-like IONF@CuS NPs were internalized in primary human mesenchymal stem cells (hMSCs), selected as a resourceful and versatile model that provides fine biocompatibility information on long-term culture. The CuS and IONF@CuS NPs were incubated for 4 h with hMSCs at Cu concentrations ranging from 0.1 to 1.6 mM. TEM images show the two stages of internalization. In Figure 2A and B, respectively CuS and IONF@CuS NPs can be seen close to the outer cell membrane, just before their internalization, which is obtained on the 2D culture in a nonspecific way. Figure 2C−F show both NPs accumulated within the endosomes, with their structural architecture still intact. Additional images are presented in Figure S4 and Figure S5. In the case of IONF@CuS NPs, the iron oxide core is easily recognizable with its nanoflower-like shape and 24 nm size compared to the surrounding CuS, which appears bigger, forming a hollow shell, as can be seen from the thin longitudinal sectioning of the samples (40 nm slices; Figure 2B and F). As emerged from elemental analysis (Figure S6), NP internalization increases with the incubation concentration for both nanoformulations. Once the nanoassemblies were internalized, high-density collected cells (250 000 cells in 10 $\mu$L, at different intracellular doses) were exposed to photothermia, in the same configuration (volume and laser power density) as previously achieved for aqueous dispersions (Figure 1). Heating efficiency in the cell environment was found to be similar for both CuS and IONF@CuS NPs (Figure 2G and H) and in the same range as obtained in water (Figure 1D). The photothermal potential of CuS-based NPs is thus similar in an aqueous dispersion or within cells.

**Biological Responses Using High-Content Imaging.** Results of cytotoxicity analyses of cellular interaction with the different NPs for 72 h investigating cell viability, mitochondrial reactive oxygen species (MitoROS), and the size of the mitochondrial network are presented in Figure 3. Representative images of the InCell analysis experiment for viability and MitoROS are presented in Figure 3D and Figure S7. Altogether, these results indicate that CuS NPs induce toxic effects only at the highest concentrations (Figure 3A). The level of observed cell death was accompanied by only a marginal increase in MitoROS (Figure 3B), while mitochondrial area (an indicator for mitochondrial stress) displayed a significant reduction in size of the cellular mitochondrial network (Figure 3C). The latter indicates a clear increase in mitochondrial stress, at high concentrations, but this does not seem to be linked to the generation of ROS.

**Long-Term Impact on Stem Cell Spheroids.** In order to perform longer-term toxicity assessment, stem cells labeled with CuS or IONF@CuS NPs (incubated at extracellular [Cu] = 0.4 mM) were cultured as spheroids for 21 days (Figure 4A). This 3D model is commonly used for the chondrogenic differentiation of stem cells, which is initiated by both the 3D organization of the cells and the addition of specific culture conditions. It results in an important production of


https://doi.org/10.1021/acsnano.1c00567
ACS Nano XXXX, XXX, XXX−XXX

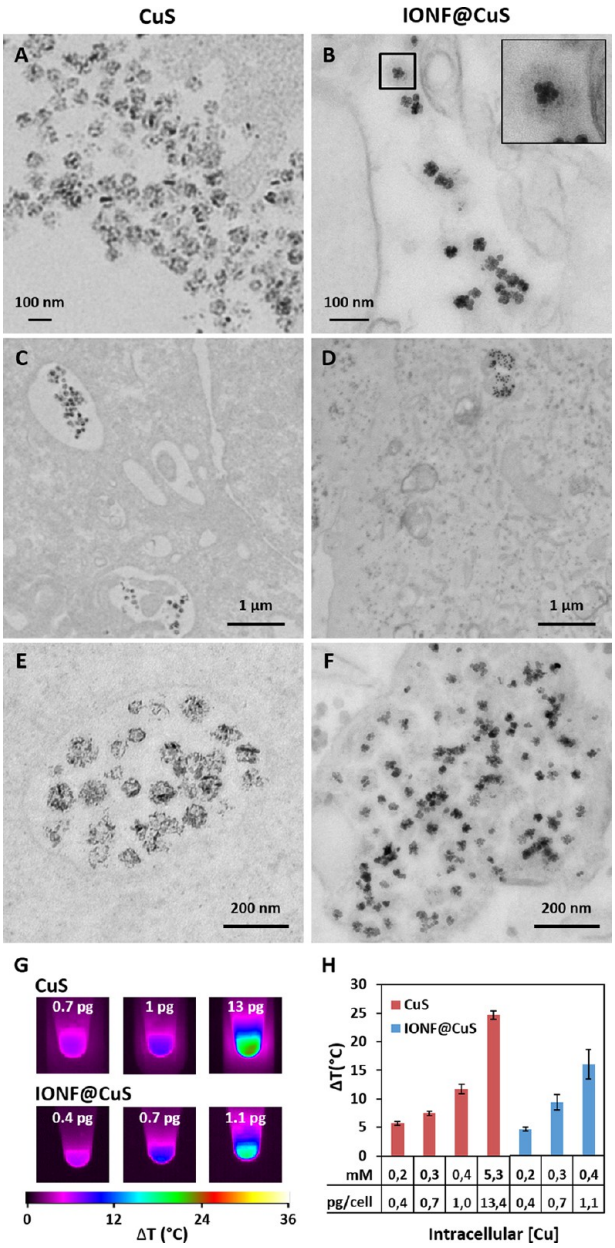


**Figure 2. NP internalization in primary stem cells. (A−F) TEM micrographs showing CuS (A, C, E) and IONF@CuS (B, D, F) nanoassemblies upon 4 h incubation with hMSCs at a Cu concentration of 0.5 mM. Some nanoassemblies are still visible at the cell outer membrane before endocytosis (A, B). Most of the nanoassemblies were however already found inside endosomes, where they appear still intact and highly accumulated (C, D, E, F). (G) Representative IR thermographic camera images of a nanoassembly-containing cell suspension (250 000 cells in 10 $\mu$L) after 5 min of 1064 nm laser exposure, at different doses of Cu. For the CuS (top), the three conditions correspond to extracellular incubation at [Cu] = 0.2, 0.4, and 1.6 mM, resulting in intracellular Cu amounts of 0.7, 1, and 13.4 pg Cu per cell, respectively. For the IONF@CuS (bottom), they correspond to [Cu] = 0.1, 0.2, and 0.4 mM, resulting in intracellular Cu amounts of 0.4, 0.7, and 1.1 pg Cu per cell, respectively. (H) Average heating of CuS and IONF@CuS treated hMSCs upon 4 h of incubation, plotted against their intracellular mass of Cu in pg per cell (*x*-axis, bottom) or the resulting molar concentration of Cu in the 10 $\mu$L cell dispersion (*x*-axis, top).**

extracellular matrix (*e.g.*, collagen II, aggrecan). Importantly, under this setup, cells can remain viable in culture for extensive time frames (even months) without dividing, allowing one to assess the long-term biological impact in a quantitative manner.

Representative TEM images taken at day 21 show that the cells labeled with CuS-based NPs have produced an organized extracellular matrix (Figure 4B), a clear sign of their advanced stage of differentiation. Histology images also confirm an abundance of proteoglycans within these CuS-incorporated spheroids similar to control spheroids, as indicated by positive toluidine blue staining (Figure 4C). Gene expression of cartilage-specific constituents (aggrecan and collagen II) was assessed by qPCR for the spheroids labeled with IONF@CuS NPs and shows an increased expression over time, similar to the control at day 21, confirming the chondrogenic differentiation of the cells (Figure S8). Overall, the intracellular presence of CuS-based NPs appears not to hinder the typical biological maturation of the stem cell spheroids.

**Long-Term Expression of Oxidative Stress and Metal Ion-Related Genes.** Biological outcomes of the internalization of CuS and IONF@CuS materials in stem cells cultured as spheroids in the long-term (up to 21 days) were assessed by measuring the expression of genes involved in the oxidative stress response and in copper and iron metabolisms (Figure 5). First, Figure 5A shows the expression of GLRX and SOD1 (encoding for glutaredoxin and superoxide dismutase 1, respectively), both involved in the antioxidant defense system, and of NOX2-$\alpha$ (encoding for NADPH oxidase 2), involved in ROS production. The expression of these oxidative stress related genes is not impacted by the presence of the CuS-based NPs. This supports the previous findings (Figure 3B) that no significant mitochondrial ROS were produced. Figure 5B evidences next that most of the copper- and iron-related genes were not upregulated, except for CP, encoding for ceruloplasmin, one of the most important copper carriers also involved in iron metabolism. By contrast, three genes encoding for metallothioneins (involved in the homeostasis of heavy metals, such as copper) are upregulated in a time-dependent manner after exposure to CuS and IONF@CuS (Figure 5C, D, and E). For the IONF@CuS, upregulation is maximal at day 3 and progressively returns to control levels over time, for all the isoforms analyzed (MT1E, MT1X, and MT2A). For CuS NPs, upregulation is less important at day 3, but remains sustained for longer duration. Hence, metallothionein gene expression is induced after exposure to both formulations of CuS-based nanomaterials.

Overall, this analysis provides insights into Cu and Fe metabolic pathways. First it suggests a role of the metallothioneins in the cellular response to Cu-based materials. The upregulation of CP for both CuS and IONF@CuS is consistent with its role not only as Cu transporter but also for Fe.[42] The particular case of ATP7A is also relevant, with an upregulation only for IONF@CuS. ATP7A encodes for the copper-transporting ATPase 1 that has for a main function the transport of Cu, and potentially Fe, across the cell membrane, and is thus related to cellular ion levels.[43]

**Structural Transformations Observed at the Nanoscale by Electron Microscopy.** TEM observations were undertaken throughout the 21 days of spheroid maturation. They evidenced that the integrity of the nanoassemblies is rapidly affected by the biological environment, with structural modifications already starting at the third day of spheroid


https://doi.org/10.1021/acsnano.1c00567
ACS Nano XXXX, XXX, XXX−XXX

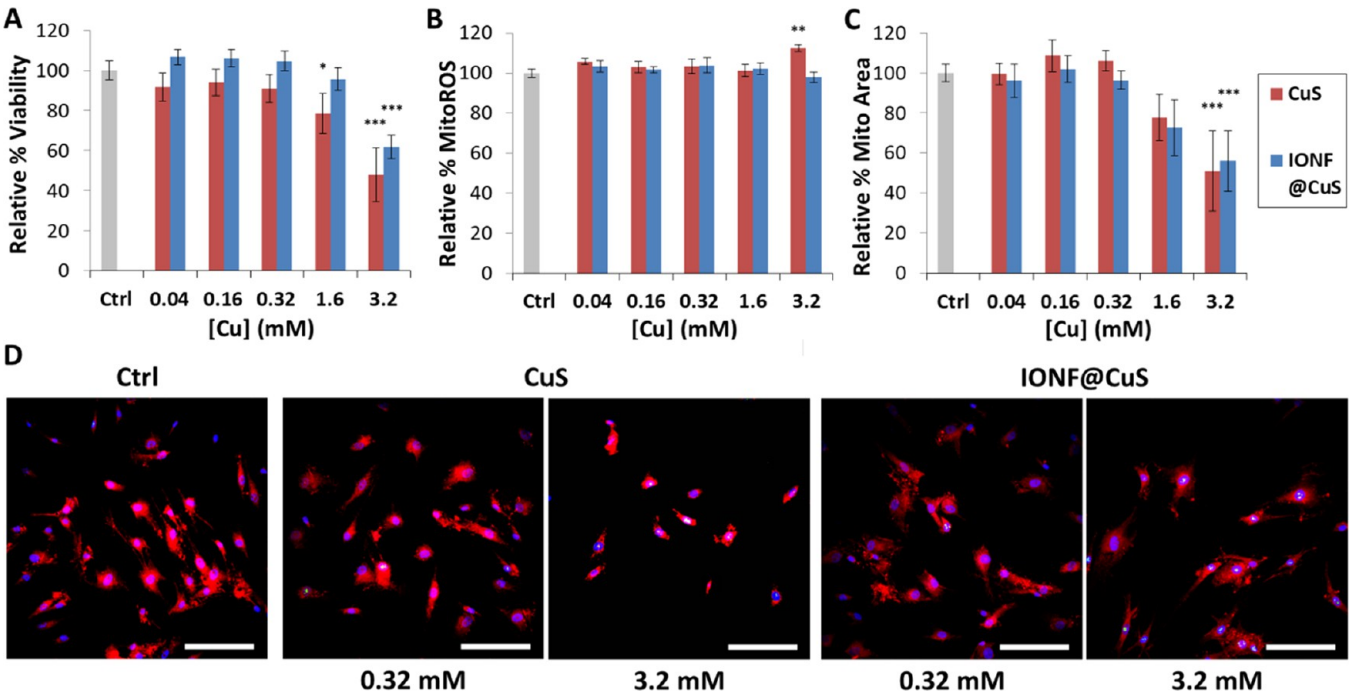


**Figure 3. Nanotoxicity screening results of hMSC exposed to various concentrations of CuS and IONF@CuS NPs for 72 h. (A) Biocompatibility analysis, (B) mitochondrial ROS, and (C) size of the mitochondrial network of hMSCs treated for 72 h with CuS and IONF@CuS at concentrations ranging from 0.04 to 3.2 mM of Cu and relative to untreated control cells (*$p < 0.05$, **$p < 0.01$, and ***$p < 0.001$). (D) Representative merged images of the hMSCs treated with CuS and IONF@CuS nanoassemblies at 0.32 and 3.2 mM of Cu. Nuclei are stained in red (Hoechst), and dead cells' nuclei are counter-stained in green (as light green spots). For the 3.2 mM conditions, many nuclei appear green labeled. Mitochondrial network stained in red (MitoTracker Red CMXRos) (Scale bar = 200 $\mu$m).**

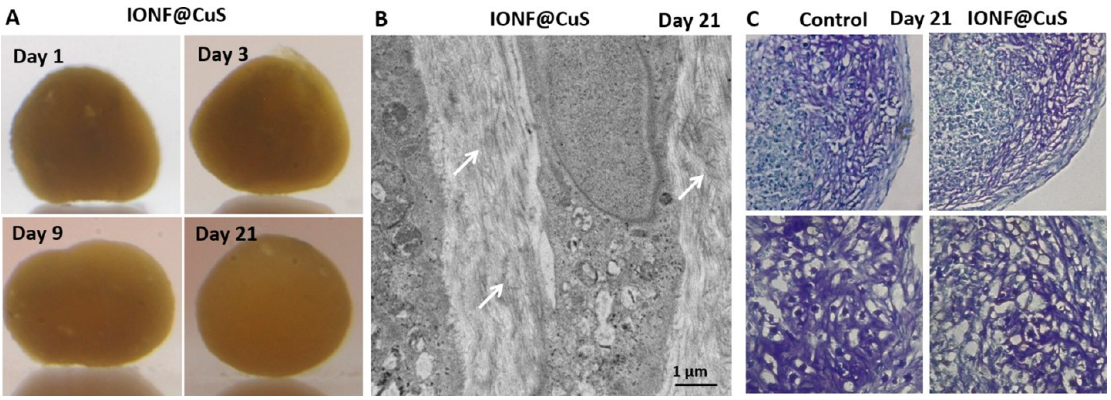


**Figure 4. Formation of spheroids from stem cells loaded with CuS-based NPs for long-term culture. (A) Representative photographs of spheroids made of stem cells loaded with IONF@CuS NPs (4 h of incubation at day 0, with 0.4 mM Cu). The spheroids become more cohesive and spherical during the 21-day culture period. (B) TEM image of a spheroid harvested and sectioned at day 21 showing the presence of a dense extracellular matrix in between the cells (white arrows). (C) Histological images of spheroids fixed and sectioned at day 21 and stained with toluidine blue. A similar staining is obtained for the control (left) and the IONF@CuS condition (right), indicating the abundance of proteoglycans in both conditions.**

maturation (day 3), both in the presence and in the absence of the IONF core (Figure 6, panels A–D). At this stage, some lysosomes still contain intact NPs, while others hold nanostructures resembling the initial nanoassemblies but disassembled into smaller units, with the IONF core also dismantled in the case of IONF@CuS (Figure 6C and D). Additional TEM images are shown in Figure S9 and Figure S10. After 21 days (Figure 6, panels E–L) absolutely no intact assemblies can be detected within the cells anymore. By contrast, neo-formed nanostructures can be clearly seen in lysosomes, generally leaned against the internal side of the membrane, in a "hair-like" manner. Similar additional images (day 9 and day 21) are shown in Figure S11 and Figure S12. Importantly, energy-dispersive X-ray spectroscopy (XEDS) elemental analysis of the transformed nanostructures at day 21 confirmed the presence of copper along the membrane of lysosomes (Figure S13). Interestingly, only for the IONF@CuS condition could we also detect small 5–7 nm NPs, that we identify as iron deposits in 5–7 nm ferritins previously observed after degradation of iron oxide nanoparticles.[23,30,31] In summary, both CuS and IONF@CuS nanoassemblies undergo a profound morphological reshaping inside the lysosomes, which occurs in close association to the inner side of the lysosomal membrane, for the Cu processing.


https://doi.org/10.1021/acsnano.1c00567
ACS Nano XXXX, XXX, XXX–XXX

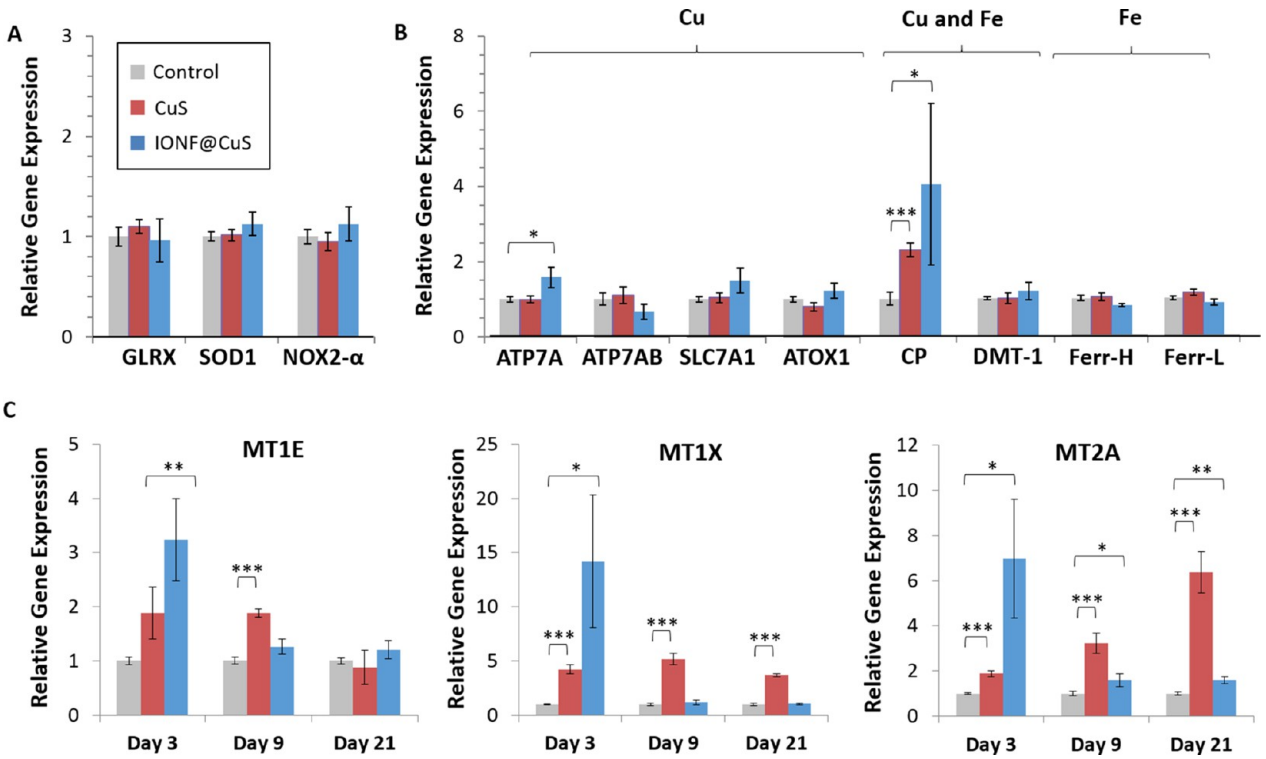


**Figure 5. Impact of the internalization of CuS or IONF@CuS on the expression of genes involved in (A) oxidative stress (day 9), (B) copper and iron metabolism (day 9), and (C−E) metallothioneins (MT1E, C; MT1X, D; MT2A, E). Gene expression was normalized to RPLP0 mRNA and expressed relative to the average values of nonlabeled spheroids harvested the same day (control). Significance is indicated as follows: *$p < 0.05$, **$p < 0.01$, and ***$p < 0.001$.**

Finally, it is important to emphasize that the *in vivo* complexity is only partially reproduced at the cell culture level. We therefore included an *in vivo* exploration of the IONF@CuS NPs fate at the organism level by injecting them intravenously in mice, harvesting the liver 1 day after the injection or 22 days later and postprocessing it for TEM imaging. The corresponding images, shown in Figure S14, evidence very similar structures to the ones observed at the cellular level.

**Photothermal Potential of the Biotransformed NPs.** The spheroids containing intact NPs (day 1) and processed ones (from day 3 to day 21) were exposed to a NIR laser (Figure 7). Overall, seven independent incubation conditions were tested, corresponding to three and four different extracellular doses for IONF@CuS and CuS NPs, respectively. Each time point corresponds to spheroids ($n = 6$) that have been fixed after 1, 3, 9, or 21 days of maturation. Unexpectedly, the photothermal heating efficiency was globally kept constant during the course of spheroid maturation for all the tested doses. Figure 7A and D show representative IR images of the heating at the first (day 1) and last (day 21) time point. A complete IR panel including also images at day 3 and day 9 can be found in Figure S15. Figure 7B and E present the average temperature increases $\Delta T$ over time. All data point out the stability of the photothermal potential of the CuS-based nanoassemblies. For all conditions, the quantity of copper (and iron) within the spheroids remains unchanged over time (Figure 7C and F), direct proof that the spheroids generally do not lose labeled cells nor eject nanomaterials or copper ions. We also tested the photothermal potential of CuS NPs dispersed in culture medium at 37 °C, without cells, for 7 days. Results are shown in Figure S16 for different concentrations, clearly demonstrating a significant reduction of the photothermal efficiency, over 30%, in 1 week of incubation.

Overall, it appears that despite the massive intracellular structural modification of the CuS and IONF@CuS NPs over weeks in stem cells, their heating potential is exceptionally conserved throughout the analysis period, in a consistent manner at all doses tested.

**Magnetometry and X-ray Absorption Spectroscopy at the Spheroid Level Reveal Degradation of the Magnetic Core but No Change in Cu Chemical State.** Magnetometry was performed on the IONF@CuS spheroids, to quantitatively detect the magnetic signature of the IONF magnetic core inside the cells over time, as an indicator of its integrity. As shown in Figure 8A (single spheroid magnetization curves at room temperature) and Figure 8B (average of spheroid saturation magnetization), a sharp reduction of the magnetization is already experienced 1 day after IONF@CuS internalization. The magnetic signal then remains very low from day 3 to day 21, demonstrating that the magnetic core is totally degraded.

X-ray absorption spectroscopy (XAS) of the spheroids at the Fe K-edge in the X-ray absorption near-edge structure regime (XANES) (Figure 8C) confirmed the degradation of the IONF magnetic core upon cellular uptake. Right after internalization in cells, IONFs were identified as maghemite by spectrum comparison with iron oxide references. Besides, the spectrum matches perfectly the one obtained before internalization, for IONFs dispersed in water (see also Figure S17A). By contrast, after 21 days, although the Fe ions remained in the +3 oxidation state, the spectra obtained evolve to a ferrihydrite-like structure and could be modeled with a high content of ferrihydrite (80%) over maghemite (Figure S17B). It confirms


https://doi.org/10.1021/acsnano.1c00567
ACS Nano XXXX, XXX, XXX−XXX

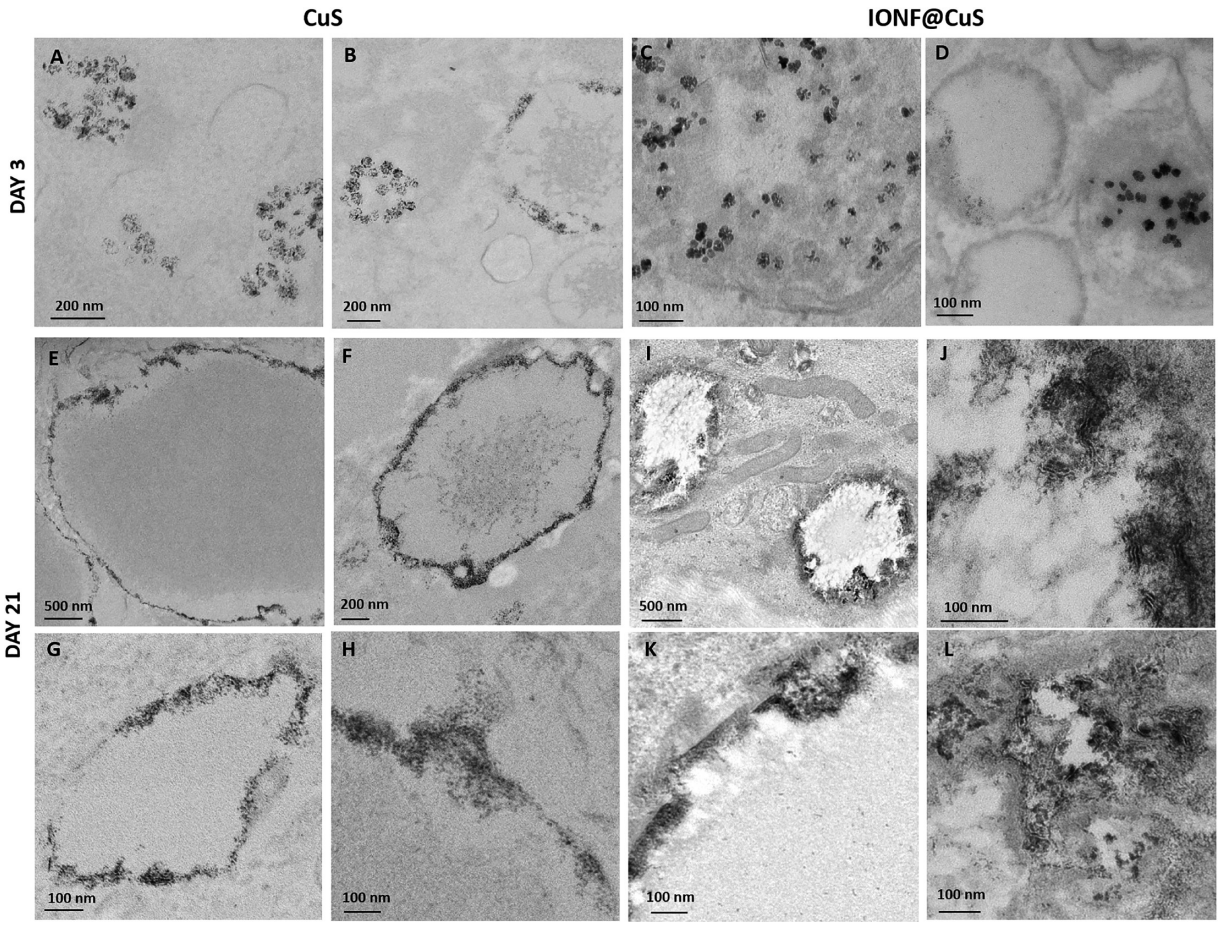


**Figure 6. TEM study of the intracellular structural transformation of nanoassemblies over time. Representative TEM images at day 3 for CuS (A, B) and IONF@CuS assemblies (C, D) show the presence of both still intact nanoassemblies and their much smaller degradation products. At day 21 of spheroid maturation, no original nanoassemblies are visible for both CuS (E−H) and IONF@CuS (I−L), while the lysosome inner membrane appears decorated with nanomaterial deposits, reshaped in smaller "hair-like" structures.**

that the degradation products issued from the magnetic core are stored within the ferritin protein as ferrihydrite, as already reported for the degradation of magnetic NPs alone.[30,31] By contrast, XANES analysis of the spheroids at the Cu K-edge (Figure 8D) demonstrates no change for the chemical phase and environment of Cu over time. Moreover, the XANES spectrum of IONF@CuS NPs dispersed in water displays identical edge positions and spectral features to those obtained in cell spheroids at all maturation durations. A fit using Cu-based reference compounds yielded a composition of mainly CuS phase (Figure S17C and D). This is in total agreement with the preservation of the photothermal potential and provides the unequivocal evidence of the massive intracellular transformation of the nanoassemblies into CuS biologically reshaped materials with the same structural chemistry and, thus, physical photothermal properties.

**Maintenance of the Therapeutic Programmed Tasks in a Cancer Model.** The stem cell spheroids, made of primary human mesenchymal stem cells, were used as a model to enable a long-term study of the intracellular remodeling of the CuS NPs, as well as to evaluate the biological impact of the NPs on healthy cells. Nevertheless, the photothermal property of CuS is usually used to treat diseases, for example, to kill tumor cells. Within the spheroids, the stem cells stop dividing and create a rich extracellular matrix, which allows them to be kept viable over months; by contrast, highly proliferating cancer cells are more challenging to culture in 3D culture in the long-term. Yet, we managed to transfer the stem cell spheroid model to glioblastoma cancer cells, which successfully formed 3D spheroids of similar size and number of cells and were maintained viable over 9 days (Figure 9A). Two doses of CuS NPs were investigated, corresponding to 0.5 and 0.9 pg of Cu per cell, in the same range as what was obtained in stem cells. The intracellular heating performances of the CuS NPs were maintained over the 9 days, with heat measurements performed at days 1, 3, 6, and 9. This is evidenced in Figure 9B, C, and D, showing typical IR images of single spheroid heating, typical temperature elevation curves for each dose and each measurement day, and a temperature increase (at plateau) averaged over five independent spheroids, as a function of time. Importantly, these series of measures were achieved starting from 37 °C, with laser exposure at low power density (0.3 W/cm$^2$), totally approved for clinical use, and for 10 min, a duration typically used for photothermal cancer therapy. With these settings, the preservation of the heat generation over time perfectly translated into a conserved therapeutic efficacy, as spheroid viability after laser exposure at days 1, 3, 6, and 9 was systematically decreased to 60% and 30% compared to the nonexposed control spheroids, for 0.5 and 0.8 pg of Cu per cell, respectively.

**Hypothetical Mechanism.** The data presented here provide insights into the landscape of intracellular reshaping


https://doi.org/10.1021/acsnano.1c00567
ACS Nano XXXX, XXX, XXX−XXX

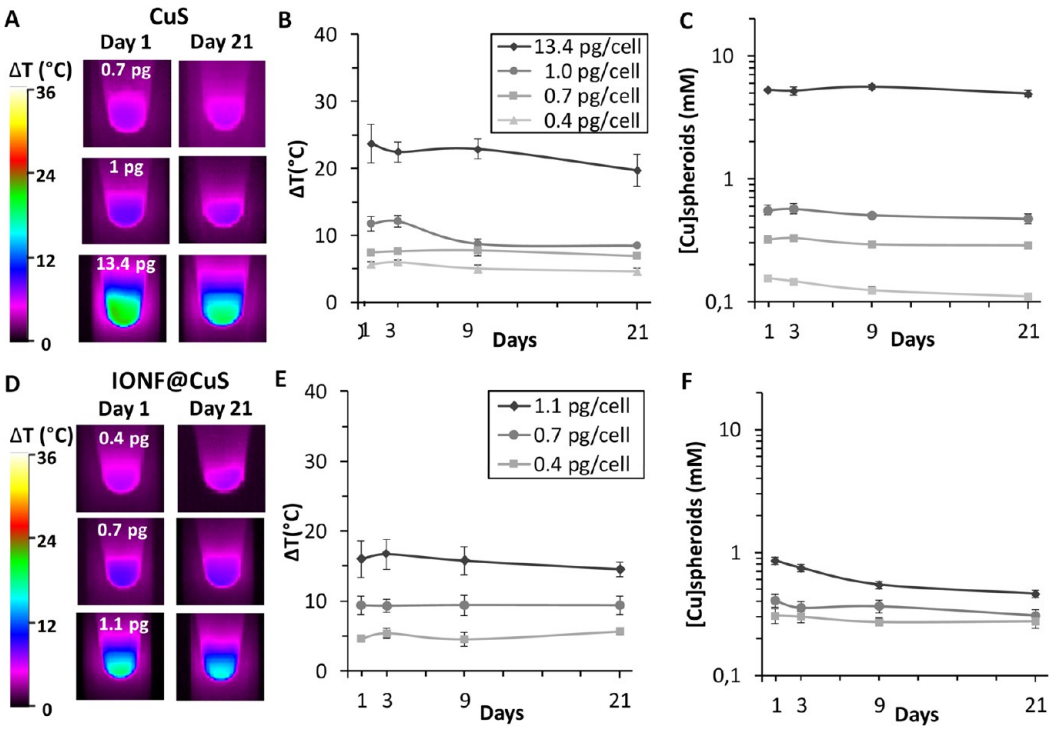


**Figure 7. Laser-induced photometric study on CuS and IONF@CuS NP-containing spheroids over time. A and D show typical IR images of three concentrations of CuS- and IONF@CuS-treated spheroids, respectively, at day 1 and 21 of spheroid maturation. Images were taken after 5 min of 1064 nm laser irradiation at 0.3 W cm$^{-2}$ (heating plateau achieved at 1−2 min of laser application). B and E present the average time plots of the heating efficiencies for all incorporated doses for spheroids treated with CuS (B) and IONF@CuS (E) at days 1, 3, 9, and 21 of spheroid maturation. C and F present [Cu] measurements obtained by ICP of the 10 μL solution containing the individual CuS- (C) and IONF@CuS-containing (F) spheroids.**

of functional nanomaterials, with the evidence that a nanoparticle can be significantly bioprocessed and transformed into different shapes and sizes while maintaining its photothermal function. This behavior was observed only for copper sulfide material, while magnetic cores were already processed to nonmagnetic after a few days as demonstrated by magnetic measurements and XAS. Such differences in cell bioprocessing of both materials may have different origins including the low solubility of metal sulfides compared to metal oxides, the differences in size and shape, but also the differences in cellular management of both metal ions, where Fe is typically metabolized rapidly after cellular uptake.[44] Naturally, Fe is transported from the outside of the cell to the inside by transferrin, which, after binding to the transferrin receptor, ends up in endosomes/lysosomes compartments. The receptor can recycle back to the cell membrane, where the Fe ion can bind small molecules such as citrate that will aid in its solubilization and transport it out of the endosomes into the labile iron pool of the cell.[45] For Fe brought inside the cells *via* NPs, it is generally the same pathway, where the NPs sequestered in endosomes are gradually degraded and free Fe ions are transported out of the endosomes into the cytoplasm.[46] For copper, the process is different and less understood. Naturally, Cu enters the cells mainly *via* the copper transporter 1 (CTR1) and is immediately linked to one of its chaperones, such as copper chaperone for SOD (CCS) or Sco1, an enzyme involved in the synthesis of cytochrome *c* oxidase.[47] Cu can be stored at low levels in metallothioneins, but overall, transport of Cu ions from endo- and lysosomes toward the cytoplasm is very limited, as it does not occur naturally. For Cu-containing NPs, this poses an entirely different scenario, in which the cells are not equipped to deal with excess levels of Cu ions in their endosomal compartments. CuO NPs, which typically dissolve quite quickly, result in free Cu ions already present in the cell medium and cellular uptake of excess Cu ions that can lead to cell death.[48] Alternatively, the low solubility of CuS and the small contact time during incubation allowed the internalization of the CuS-based nanostructures, still intact, in the endosomes of the cells, on the first day.

Moreover, TEM observation of these CuS confirmed their porous and polycrystalline architecture, made of tiny particles 7−11 nm in diameter. Such tiny crystals are organized in a hollow porous morphology resulting from the Kirkindall effect in the presence of polyvinylpyrrolidone (PVP). The degradation of similar hollow CuS NPs in different physiological buffers including PBS, RMPI, and DMEM was investigated by Ortiz de la Solorzano *et al.*[41] at 37 °C, who showed their dissolution into water-soluble sulfate-based copper species. This dissolution led to the decrease of the NIR absorption peak with almost a total disappearance after 13 days. Consequently, it is expected that the disappearance of the NIR absorption should lead to a loss of the photothermal properties, which was not observed in our investigation for both types of nanoparticles in cells. These results are in good agreement with XAS data and indicate that the degradation of CuS in the endosomes by dissolution of water-soluble copper species is not the predominant mechanism, at least on the scale of 29 days. At day 3, in addition to intact hollow structures, smaller CuS units are also observed by TEM, and these units decorate the internal membrane of the endosomes. Interestingly, despite the presence of such dissociated structures, no


https://doi.org/10.1021/acsnano.1c00567
ACS Nano XXXX, XXX, XXX−XXX

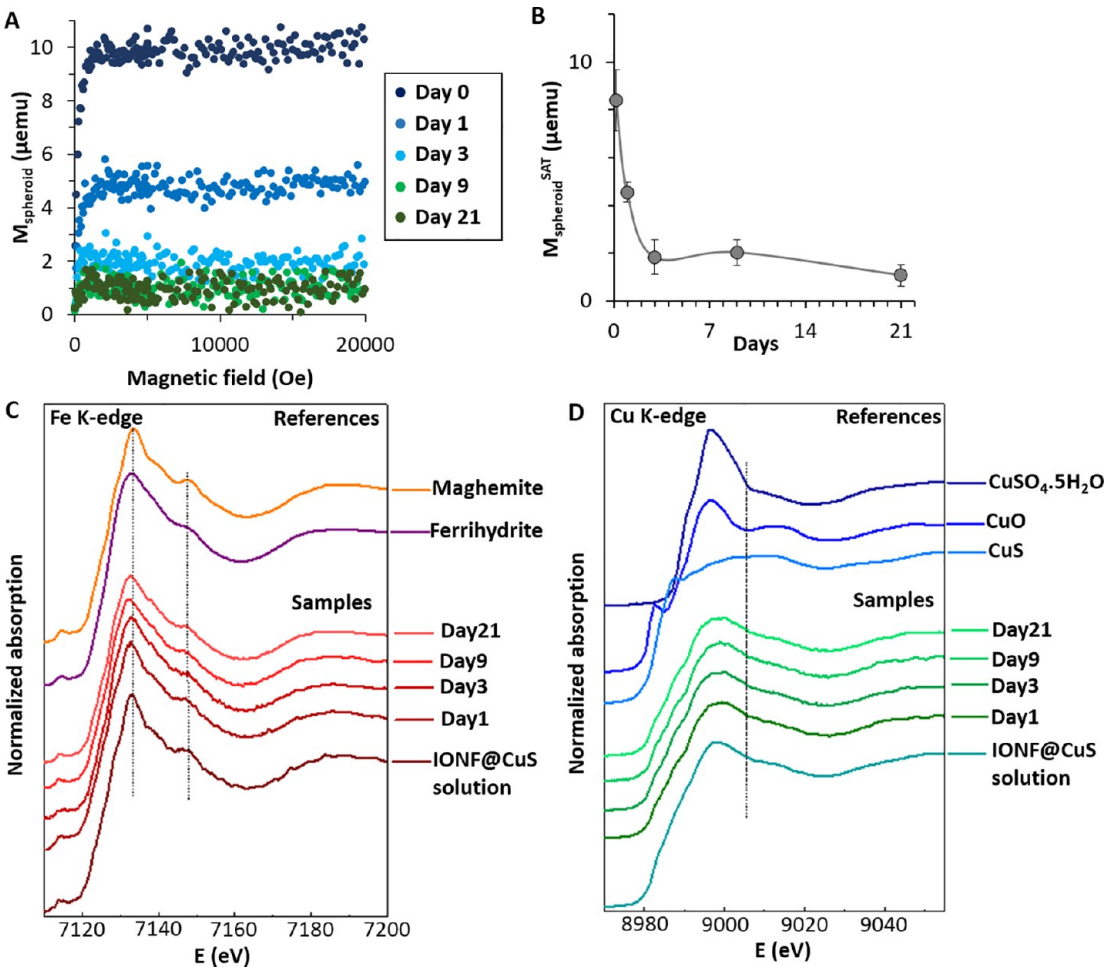


**Figure 8. Structural characterization of IONF@CuS NPs processed by the spheroids from incubation day (day 0) to 3 weeks of maturation (day 21), taking advantage of the magnetic core as an additional integrity tracer. (A) Typical magnetometry curves for single spheroids at room temperature over time. (B) Magnetization at saturation averaged over four independent spheroids at each time point (total of 20 spheroids analyzed). (C) XANES spectra at the Fe K-edge of iron oxide references ($\gamma$-$Fe_2O_3$ (maghemite) and $Fe_2O_3 \cdot 0.5H_2O$ (ferrihydrite)), IONF@CuS NPs incubated from day 1 to day 21, and IONF@CuS NPs dispersed in water. (D) XANES spectra at the Cu K-edge of copper-based compound references ($CuSO_4 \cdot 5H_2O$, CuO, CuS), IONF@CuS nanoassemblies incubated from day 1 to day 21, and IONF@CuS NPs dispersed in water.**

change in photothermia or chemical phase was observed. Consequently, we attributed the formation of such free units to the disassembly (by dissolution of PVP) of the tiny nanoparticles from the shell of CuS. After coating with positively charged endosomal proteins they undergo interaction and accumulation at the negatively charged lysosomal inner membrane. A comparable disintegration mechanism has been observed *in vivo* in blood plasma for similar hollow shells by Guo *et al.*[40] At day 21, TEM showed that no intact CuS nanostructures remained for both types of nanostructures, while the lysosome inner membrane appeared decorated with 4−8 nm nanoparticles organized in a hair-like structure. Such structures are copper-based, as confirmed by XEDS analysis. Therefore, we may hypothesize that these structures were generated by continuous disintegration of the CuS over time and reorganization of the tiny subunits released.

At high concentrations, the nanohybrids induced mitochondrial stress but no ROS generation, while Cu-based nanoparticles are typically associated with the induction of ROS.[36,49] The lack of mitochondrial ROS also reflects a low level of dissolution of CuS. However, the observed mitochondrial stress and the increasing activity of genes related to copper suggest that free copper species are released during the bioprocessing of the nanostructures. Indeed, XAS analysis shows that the CuS shell is composed of a mixture of CuS and CuO phases and free $CuSO_4 \cdot 5H_2O$. Given the higher solubility of CuO compared to CuS also established in cells, we may hypothesize that, upon the nanomaterial bioprocessing, free CuO species are released upon the nanomaterial bioprocessing and that they are stored in the copper-related proteins.

Concerning the stability of photothermal potential upon the degradation of the CuS-based NPs into small structures, it is difficult to establish a clear reason, as the origins of absorption in copper sulfide remain poorly understood and are still a subject of debate. While some associate this NIR absorption to d−d transition of $Cu^{2+}$ ions, which is not affected by the solvent or the surrounding environment, others attribute such a behavior to a plasmonic effect generated by free hole oscillations.[37,38] In this case the effect of morphology on the localized surface plasmon resonance is not clearly understood, and it seems that the morphology has less influence on their plasmon oscillation mode with respect to the composition.[38] In all cases we can attribute the conservation of the photothermal


https://doi.org/10.1021/acsnano.1c00567
ACS Nano XXXX, XXX, XXX−XXX

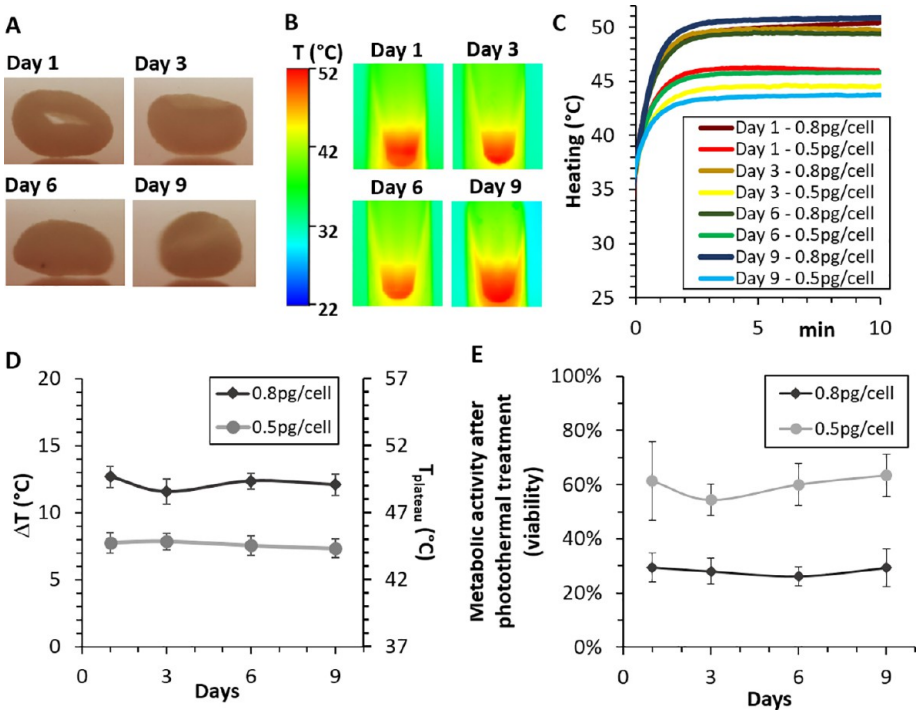


**Figure 9. Preservation of photothermia and subsequent therapeutic potential in a glioblastoma spheroid model. (A) Representative photographs of single spheroids made of 2.5 × $10^5$ cancer cells containing CuS NPs at a dose of 0.8 pg of Cu per cell, at days 1, 3, 6, and 9. (B) Typical IR images of cancer spheroids (loaded with CuS NPs at 0.8 pg of Cu per cell) in a 0.5 mL tube (10 $\mu$L volume), at days 1, 3, 6, and 9 of spheroid maturation, upon 10 min of laser irradiation at 0.3 W $cm^{-2}$. (C) Typical heating curve for single spheroids, at each day (1, 3, 6, and 9) and for the two doses (0.5 and 0.8 pg of Cu per cell). (D) Plateau temperature, expressed as temperature elevation (left vertical axis) and absolute temperature (right secondary axis), averaged over five independent spheroids, as a function of time. (E) Metabolic activity (Alamar blue assay) of the spheroids ($n$ = 5 per day and per dose), measured 24 h after photothermal treatment, expressed in % compared to nontreated control spheroids ($n$ = 5 per day and per dose).**

potential to the preservation of the chemical composition, as confirmed by XAS performed over days on the units formed after disintegration of the original CuS nanomaterials.

These results show clearly that multifunctional materials with predefined properties can be bioprocessed by cells into new reshaped biological forms, which may present a high biocompatibility while maintaining their functionalities and their programmed therapeutic tasks.

## CONCLUSION

Herein, we studied the effect that a long intracellular exposure of CuS-based nanomaterials could have on both their own physical functionalities and on the biology of the stem cells exposed. CuS were produced as nanoassemblies, without (CuS) and with a magnetic core (IONF@CuS), internalized in stem cells further assembled in spheroids to allow long-term 3D culture. Overall, the CuS and IONF@CuS NPs did not trigger an adverse biological response either immediately (over the cell viability, oxidative stress), or in the longer-term (over stem cell differentiation, oxidative stress, iron and copper metabolism). However, the nanoassemblies were massively transformed inside the endosomes of the cells, with only few intact structures observed already after 3 days of cellular processing. These transformations were quantitatively confirmed by magnetometry by the disappearance of the spheroid magnetism initially provided by the IONF core and confirmed by XAS synchrotron measurements, revealing the transformation of maghemite into ferrihydrite over time. The magnetic core was, thus, totally degraded by the cells and stored within the ferritin protein, as generally observed for magnetic NPs alone. This magnetic degradation reflects the disassembling of the hybrid IONF@CuS structure, making it possible for the lysosomal harsh environment to access the core and degrade it. However, the loss of magnetism was not associated with a comparable loss of the photothermal potential of the spheroids over time, provided by the CuS physicochemical structure of the metal chalcogenide semiconductor. The demonstration by XAS that the copper chemical phase remained the same during the whole 3 weeks of the spheroid maturation period further confirmed their functional stability. The copper sulfide nanoassemblies were therefore reshaped by the cells, triggering a process of nontoxic metabolization in which the cellular environment managed to transform the materials into smaller and stable structures with the same high photothermal potential. Since these nanoparticles are devoted to therapeutic applications, the photothermal follow-up was also performed on spheroids made of cancer cells. The photothermal potential and its related therapeutic function were maintained all through the cancer spheroid maturation (over 9 days). In order to implement efficient theranostic applications, it appears pivotal to study the balance between biocompatibility, degradation, and bioprocessing while maintaining their physical properties. Herein, we demonstrate that a theranostics nanomaterial can undergo a severe clear cell-mediated breakdown but still maintain its programmed tasks after intracellular processing.


https://doi.org/10.1021/acsnano.1c00567
ACS Nano XXXX, XXX, XXX−XXX

## MATERIALS AND METHODS

**Materials.** All reagents were of analytical purity and used without further purification. Iron(II) chloride tetrahydrate ($FeCl_2 \cdot 4H_2O$, 99%), sodium hydroxide (NaOH, 99.99%), diethylene glycol (DEG, 99%), *N*-methyldiethanolamine (NMDEA, 99%), nitric acid ($HNO_3$, 70%), copper(II) nitrate hemi(pentahydrate) ($Cu(NO_3)_2 \cdot 2.5H_2O$, ≥99.99%), polyvinylpyrrolidone (PVP, $M_w$ 55 kDa), poly(ethylene glycol) methyl ether thiol (PEG-SH, $M_w$ 2 kDa) hydrazine hydrate (55%), ammonium sulfide solution ($(NH_4)_2S$, 20%), sodium cacodylatetrihydrate (≥98%), glutaraldehyde solution (25% in $H_2O$), and formalin solution (10%) were purchased from Sigma-Aldrich (France). Iron(III) chloride hexahydrate ($FeCl_3 \cdot 6H_2O$, 99%) and ethanol were obtained from VWR (France). Live−Dead Green dead cell and MitoTracker Red CMXRos were purchased from Life Technologies (Thermo Fisher, Belgium).

**Iron Oxide Nanoflower Core.** IONFs were synthesized using a modified polyol synthesis as previously described.[50] In brief, the iron precursors were solubilized in a DEG and NMDEA mixture (1:1 v/v) and heated to 220 °C for 2.5 h to obtain the alkaline hydrolysis. The obtained magnetic nanoflowers were cleaned with ethanol and ethyl acetate and treated with 10% nitric acid to complete the oxidation. They were then redispersed in water and mixed with 0.3% PVP (55 kDa) prior to the following step.

**Copper Sulfide Assembly.** The synthesis of the substoichiometric copper sulfide $Cu_{2-x}S$ assembly has been carried out in the presence or in the absence of an IONF core using a two-step reaction through a template sacrificial synthesis method, modified from ref 33. In the first step, 10 mg of cupric nitrate, $Cu(NO_3)_2$, was dissolved in 30 mL of Milli-Q $H_2O$ and mixed with 0.3 g of PVP (55 kDa) and IONF (if present) at [Fe] = 0.3 mM. After 15 min of shaking at room temperature 100 μL of hydrazine 5.5% was added rapidly in the mixture to induce the formation of $Cu_2O$ NPs. The obtained product was cleaned by centrifugation at 9000*g* for 45 min and resuspended in 30 mL of Milli-Q $H_2O$. The second step of the reaction consisted in the sulfidation of the $Cu_2O$ shell previously synthesized using 0.1 M sodium sulfide followed by heating at 50 °C for 2 h. After several washings by centrifugation and resuspension in Milli-Q $H_2O$, the surface of the nanoassemblies was PEGylated by shaking the sample overnight in the presence of PEG-SH (final concentration 10 mg/mL) at 4 °C and subsequent washing by centrifugation. These reactions resulted in the production of copper sulfide nanoassemblies (hollow) or of iron oxide nanoflower-like cores surrounded by copper sulfide nanoassemblies (IONF@CuS) when achieved in the presence of IONF (rattle-like).

**Morphological and Optical Characterization.** TEM images were obtained using a Hitachi HT 7700 TEM operated at 80 kV (Elexience, France), and images were acquired with a charge-coupled device camera (AMT). UV−vis−NIR characterization was performed with a real-time Avaspec-USB2 spectrometer. Cu and Fe concentration was determined by elemental analysis using ICP-AES (iCAP 6500, Thermo Scientific).

**Laser-Induced Thermometric Measurements.** Heating profiles of aqueous solutions were obtained by placing 10 μL of CuS or IONF@CuS dispersions at concentrations ranging from 0.5 to 40 mM of Cu in a 0.5 mL tube at a 4 cm distance from the laser source. The samples were irradiated with a 1064 nm laser at a power density of 0.3 W $cm^{-2}$ until equilibrium temperature was reached (typically in 1−2 min, measurements were performed over 5 min to be sure to measure the plateau temperature). The increase in temperature was measured using an FLIR SC7000 infrared thermal camera. The spheroids were analyzed in the same configuration. All values are reported as means of at least three separate experiments.

**Cell Culture and Nanoparticle Uptake.** Human mesenchymal stem cells were purchased from Lonza and were cultured in hMSC-basal medium at 37 °C, 5% $CO_2$, and 95% relative humidity. Human glioblastoma cells U87 were purchased from ATCC and cultured in DMEM medium supplemented with 1% (w/v) streptomycin, 1% (w/v) penicillin, and 10% (w/v) FBS. At 90% confluence, cells were incubated with the nanoassemblies diluted in serum-free RPMI medium. The copper concentration in the medium ranged from 0.1 to 1 mM. After 4 h of incubation, the medium was removed and the cells were rinsed and incubated further for 2 h in complete hMSC-basal medium to remove any noninternalized copper nanoassemblies. Then, cells were detached by trypsinization, counted, and immediately analyzed or further processed. To assess the intracellular NP content, $2.5 \times 10^5$ cells were digested in pure nitric acid for 48 h until total dissolution, diluted up to 2% $HNO_3$ in ultrapure $H_2O$, and analyzed by elemental analysis.

**Nanotoxicity Study.** For the biocompatibility assays, $1.25 \times 10^3$ or $2.5 \times 10^3$ cells per well were seeded in 96-multiwell culture plates at 100 μL total volume and incubated overnight. IONF@CuS or CuS nanoassemblies at the concentrations of 0.04, 0.16, 0.32, 1.6, and 3.2 mM of Cu were dispersed in cell culture media and incubated with hMSC cells for 24 h ($2.5 \times 10^3$ cells) or 72 h ($1.25 \times 10^3$ cells). At the end of the incubation, the media was removed and fresh media was provided containing Live−Dead Green dead cell and MitoTracker Red CMXRos (Molecular Probes, Life Technologies Europe, BV, Belgium), after which the cells were further incubated for 30 min in a humidified atmosphere at 37 °C and 5% $CO_2$. Next, the cells were washed three times with PBS, fixed with 4% paraformaldehyde (PFA), and counterstained with Hoechst 33342 nuclear stain solution (Life Technologies, Belgium). Next, the plates were analyzed using the INCell Analyzer 2000 (GE Healthcare Life Sciences, Belgium), while 2000 cells per condition were acquired in triplicates using a 20× objective lens for the DAPI/DAPI (Hoechst), FITC/FITC (Live−Dead Green), and TexasRed/TexasRed (MitoTracker Red CMXRos) channels. The acquired images were processed using the InCell Investigator software (GE Healthcare Life Sciences, Belgium). Cell viability was calculated by segmenting cell nuclei and dead cells (signal crossing the threshold in the green channel overlapping with the nuclei) using the IncCell Developer software (GE Healthcare Life Sciences, Belgium). The number of live cells per each condition was calculated as the total number of nuclei counted minus the number of dead cells. The values were then normalized by the control conditions (= 100%). Finally, for mitochondrial stress, the total area of cellular mitochondria was used, while for mitochondrial ROS, the intensity of the mitochondrial stain was determined. The respective channel was segmented using the Hoechst images as seed, and the total size and intensity of the mitochondrial network were determined for each individual cell. These values were than normalized by the respective control conditions (= 100%). Results represent quantitative data for the analysis of a minimum of 2000 cells per condition. Values are presented as mean + SEM ($n$ = 3).

**Stem Cell Spheroid Formation and Characterization.** A total of $2.5 \times 10^5$ stem cells were centrifuged (1200 rpm for 5 min) in 15 mL tubes to form a pellet and cultured in order to induce cell differentiation (chondrogenesis). The cells then spontaneously formed a spheroid, which could be kept in culture for months (here up to 3 weeks of spheroid maturation). The differentiation medium was composed of high-glucose DMEM supplemented with 1% penicillin−streptomycin, 0.1 μM dexamethasone, 1 mM sodium pyruvate, 50 μM L-ascorbic acid 2-phosphate, 0.35 mM L-proline (Sigma), 1% ITS-Premix (Corning), and 10 ng/mL TGF-β3 (Interchim) and was changed twice a week. For histological analysis, spheroids harvested after 21 days of maturation were fixed overnight in 10% formalin, before paraffin inclusion and cutting. Slices that were 4 μm thick were treated with toluidine blue 0.04% for collagen staining and then analyzed by optical microscopy.

At days 1, 3, 9, and 21, the spheroids were fixed with 4% PFA for 2 h at room temperature and transferred in PBS for photothermal analysis, magnetic characterization, and elemental characterization. For the electron microscopy analysis, other spheroids at the same time points were fixed with 2% glutaraldehyde in 0.1 M cacodylate buffer for 2 h, contrasted with oolong tea extract (OTE) 0.5% in 0.1 M Na cacodylate buffer, postfixed with 1% osmium tetroxide containing 1.5% potassium cyanoferrate, gradually dehydrated in ethanol (30% to 100%), and gradually embedded in epoxy resins. Ultrathin slices (70


https://doi.org/10.1021/acsnano.1c00567
ACS Nano XXXX, XXX, XXX−XXX

nm) were collected onto 200 mesh copper grids and counterstained with lead citrate prior to being observed by TEM.

**Gene Expression Quantification by qPCR.** Total RNA was extracted from spheroids at different maturation times using a NucleoSpin RNA II kit (Macheney-Nagel). Reverse transcription into cDNA was achieved using SuperScript II reverse transcriptase (Invitrogen) with random hexamers as primers according to the manufacturer's instructions. qPCR was performed with StepOnePlus (Applied Biosystems) using the SYBR Green reagent (Applied Biosystems). The expression of reference gene RPLP0 was used as a housekeeping transcript gene. Each value is obtained by the average of at least two wells gathering a minimum of three independent repetitions. The sequences of primers used are listed in Table S1.

**Magnetometry of the Internalized IONF Core by VSM.** Cell magnetization right after IONF@CuS nanoassembly incubation and in samples fixed at different spheroid maturation times was measured by magnetometry using a PPMS device equipped with a vibrating sample magnetometer (VSM) option (Quantum Design). The analysis was performed at 300 K, between 0 and 20 000 Oe, and provides the saturation magnetization of the sample (in emu).

**XAS/Synchrotron Measurements.** XAS measurements were performed on the spheroids pooled in groups of 4 or 5 for each maturation time to increase the signal-to-noise ratio. Measurements were achieved in the XANES regime at the CRG beamline BM25-SpLine of the European Synchrotron Radiation Facilities (ESRF) in Grenoble (France). The spectra were acquired at the Fe K-edge (7112 eV) and Cu K-edge (8980 eV) at room temperature and atmospheric pressure in transmission and fluorescence modes. Metal foils of Fe and Cu elements were measured as energy calibration references. Iron oxides (as maghemite and ferrihydrite) and several copper-based materials (Cu−S−O compounds as copper sulfides, copper oxides, and copper sulfates) were chosen as standards. For each condition (at days 1, 3, 9, and 21 of maturation), a group of 3 or 4 multicellular spheroids was measured to improve the signal-to-noise ratio. XANES spectra of IONF, IONF@CuS, and CuS initial solution samples were also evaluated. Data normalization, energy calibration, and analysis of the XAS data were carried out using the Demeter software package (Athena program).[51]

**Cancer Cell Spheroid Formation and Photothermal Therapy.** In the exact same way as for the stem cells, $2.5 \times 10^5$ U87 cancer cells were pelleted and kept in complete culture medium for 9 days. At days 1, 3, 6, and 9, the spheroids (5 per day) were collected and transferred to 0.5 mL tubes (one spheroid per tube) in 10 $\mu$L of culture medium. The tubes were placed in a thermostatic device so that the sample is maintained at a temperature of 37 °C before exposure to the laser. Heating was achieved with the spheroids placed 4 cm away from the laser source (1064 nm), corresponding to a laser power density of 0.3 W $cm^{-2}$.

The samples were irradiated for 10 min. The increase in temperature was measured using an FLIR SC7000 infrared thermal camera. After laser treatment, the spheroids were transferred to a 48-multiwell plate, and each single spheroid's metabolic activity was measured 24 h later, by the Alamar blue assay, and renormalized by nontreated control spheroid values (5 control spheroids for each measurement day).

**Statistical Analysis.** All values are reported as means and standard error of the mean. Significant differences were determined using Tukey's test in one-way analysis of variance (ANOVA). * denotes a $p$-value < 0.05 (significant result), ** a $p$-value < 0.01 (very significant), and *** a $p$-value < 0.001 (highly significant).

## ASSOCIATED CONTENT

### Supporting Information

The Supporting Information is available free of charge at https://pubs.acs.org/doi/10.1021/acsnano.1c00567.

Additional nanoparticle and *in vivo* TEM images, DLS analysis, light-to-heat conversion coefficient, elemental analysis, InCell analyzer microscopy images, gene expression, STEM-HAADF and XEDS characterization, supplementary IR images, *in vitro* photothermal analysis, XANES synchrotron spectra, and the qPCR primers list (PDF)

## AUTHOR INFORMATION


### Corresponding Authors

**Ali Abou-Hassan** − *Sorbonne Université, CNRS UMR234, PHysico-chimie des Electrolytes et Nanosystèmes InterfaciauX, PHENIX, F-75005 Paris, France; Nanobiotecnología (IMDEA-Nanociencia), Unidad Asociada al Centro Nacional de Biotecnología (CSIC), 28049 Madrid, Spain;* orcid.org/0000-0002-9070-1024; Email: ali.abou_hassan@sorbonne-universite.fr

**Claire Wilhelm** − *Laboratoire Matière et Systèmes Complexes MSC, UMR 7057, CNRS and University of Paris, 75205 Paris, Cedex 13, France; Laboratoire PhysicoChimie Curie, Institut Curie, PSL Research University−Sorbonne Université−CNRS, 75005 Paris, France; Nanobiotecnología (IMDEA-Nanociencia), Unidad Asociada al Centro Nacional de Biotecnología (CSIC), 28049 Madrid, Spain;* orcid.org/0000-0001-7024-9627; Email: claire.wilhelm@univ-paris-diderot.fr

### Authors

**Alberto Curcio** − *Laboratoire Matière et Systèmes Complexes MSC, UMR 7057, CNRS and University of Paris, 75205 Paris, Cedex 13, France; Laboratoire PhysicoChimie Curie, Institut Curie, PSL Research University−Sorbonne Université−CNRS, 75005 Paris, France*

**Aurore Van de Walle** − *Laboratoire Matière et Systèmes Complexes MSC, UMR 7057, CNRS and University of Paris, 75205 Paris, Cedex 13, France; Laboratoire PhysicoChimie Curie, Institut Curie, PSL Research University−Sorbonne Université−CNRS, 75005 Paris, France*

**Emilia Benassai** − *Laboratoire Matière et Systèmes Complexes MSC, UMR 7057, CNRS and University of Paris, 75205 Paris, Cedex 13, France; Sorbonne Université, CNRS UMR234, PHysico-chimie des Electrolytes et Nanosystèmes InterfaciauX, PHENIX, F-75005 Paris, France*

**Aida Serrano** − *Spanish CRG beamline at the European Synchrotron (ESRF), F-38043 Grenoble, France; Departamento de Electrocerámica, Instituto de Cerámica y Vidrio, 28049 Madrid, Spain;* orcid.org/0000-0002-6162-0014

**Nathalie Luciani** − *Laboratoire Matière et Systèmes Complexes MSC, UMR 7057, CNRS and University of Paris, 75205 Paris, Cedex 13, France*

**Nicolas Menguy** − *Sorbonne Université, UMR CNRS 7590, MNHN, IRD, Institut de Minéralogie, de Physique des Matériaux et de Cosmochimie, IMPMC, 75005 Paris, France*

**Bella B. Manshian** − *NanoHealth and Optical Imaging Group, Department of Imaging and Pathology, KU Leuven, B3000 Leuven, Belgium;* orcid.org/0000-0002-3402-3927

**Ara Sargsian** − *NanoHealth and Optical Imaging Group, Department of Imaging and Pathology, KU Leuven, B3000 Leuven, Belgium*

**Stefaan Soenen** − *NanoHealth and Optical Imaging Group, Department of Imaging and Pathology, KU Leuven, B3000 Leuven, Belgium;* orcid.org/0000-0003-2390-3133

**Ana Espinosa** − *Nanobiotecnología (IMDEA-Nanociencia), Unidad Asociada al Centro Nacional de Biotecnología*




https://doi.org/10.1021/acsnano.1c00567
ACS Nano XXXX, XXX, XXX−XXX

(CSIC), 28049 Madrid, Spain; orcid.org/0000-0002-5626-6129

Complete contact information is available at: https://pubs.acs.org/10.1021/acsnano.1c00567

## Notes

The authors declare no competing financial interest.

## ACKNOWLEDGMENTS

This work was supported by the European Union (ERC-2014-CoG project MaTissE 648779 and ERC-2019-CoG project NanoBioMade 865629). A.V. acknowledges financial support from the CNRS through the MITI interdisciplinary programs Métallo-Mix (project BioMade), and A.E. and A.S. acknowledge support from the Comunidad de Madrid for the "Atracción de Talento Investigador" contracts (Nos. 2018-T1/IND10058 and 2017-T2/IND5395). The authors thank Christine Péchoux for the TEM imaging (platform TEM, INRA, Jouy-en-Josas), the ESRF for beam time, and the CRG beamline BM25-SpLine personnel for technical support.

## REFERENCES

(1) Giner-Casares, J. J.; Henriksen-Lacey, M.; Coronado-Puchau, M.; Liz-Marzán, L. M. Inorganic Nanoparticles for Biomedicine: Where Materials Scientists Meet Medical Research. *Mater. Today* **2016**, *19* (1), 19−28.

(2) Bakhtiary, Z.; Saei, A. A.; Hajipour, M. J.; Raoufi, M.; Vermesh, O.; Mahmoudi, M. Targeted Superparamagnetic Iron Oxide Nanoparticles for Early Detection of Cancer: Possibilities and Challenges. *Nanomedicine* **2016**, *12* (2), 287−307.

(3) Pelaz, B.; Alexiou, C.; Alvarez-Puebla, R. A.; Alves, F.; Andrews, A. M.; Ashraf, S.; Balogh, L. P.; Ballerini, L.; Bestetti, A.; Brendel, C.; Bosi, S.; Carril, M.; Chan, W. C. W.; Chen, C.; Chen, X.; Chen, X.; Cheng, Z.; Cui, D.; Du, J.; Dullin, C.; et al. Diverse Applications of Nanomedicine. *ACS Nano* **2017**, *11* (3), 2313−2381.

(4) Patino, T.; Mahajan, U.; Palankar, R.; Medvedev, N.; Walowski, J.; Münzenberg, M.; Mayerle, J.; Delcea, M. Multifunctional Gold Nanorods for Selective Plasmonic Photothermal Therapy in Pancreatic Cancer Cells Using Ultra-Short Pulse Near-Infrared Laser Irradiation. *Nanoscale* **2015**, *7* (12), 5328−5337.

(5) Espinosa, A.; Reguera, J.; Curcio, A.; Muñoz-Noval, Á.; Kuttner, C.; Van de Walle, A.; Liz-Marzán, L. M.; Wilhelm, C. Janus Magnetic-Plasmonic Nanoparticles for Magnetically Guided and Thermally Activated Cancer Therapy. *Small* **2020**, *16* (11), 1904960.

(6) Rastinehad, A. R.; Anastos, H.; Wajswol, E.; Winoker, J. S.; Sfakianos, J. P.; Doppalapudi, S. K.; Carrick, M. R.; Knauer, C. J.; Taouli, B.; Lewis, S. C.; Tewari, A. K.; Schwartz, J. A.; Canfield, S. E.; George, A. K.; West, J. L.; Halas, N. J. Gold Nanoshell-Localized Photothermal Ablation of Prostate Tumors in a Clinical Pilot Device Study. *Proc. Natl. Acad. Sci. U. S. A.* **2019**, *116* (37), 18590−18596.

(7) Martina, M.-S.; Wilhelm, C.; Lesieur, S. The Effect of Magnetic Targeting on the Uptake of Magnetic-Fluid-Loaded Liposomes by Human Prostatic Adenocarcinoma Cells. *Biomaterials* **2008**, *29* (30), 4137−4145.

(8) Soenen, S. J.; Parak, W. J.; Rejman, J.; Manshian, B. (Intra) Cellular Stability of Inorganic Nanoparticles: Effects on Cytotoxicity, Particle Functionality, and Biomedical Applications. *Chem. Rev.* **2015**, *115* (5), 2109−2135.

(9) Caracciolo, G.; Vali, H.; Moore, A.; Mahmoudi, M. Challenges in Molecular Diagnostic Research in Cancer Nanotechnology. *Nano Today* **2019**, *27*, 6−10.

(10) Chen, C.; Leong, D. T.; Lynch, I. Rethinking Nanosafety: Harnessing Progress and Driving Innovation. *Small* **2020**, *16* (21), 2002503.

(11) Carril, M.; Padro, D.; Del Pino, P.; Carrillo-Carrion, C.; Gallego, M.; Parak, W. J. *In Situ* Detection of the Protein Corona in Complex Environments. *Nat. Commun.* **2017**, *8* (1), 1−5.

(12) Mahmoudi, M.; Bertrand, N.; Zope, H.; Farokhzad, O. C. Emerging Understanding of the Protein Corona at the Nano-Bio Interfaces. *Nano Today* **2016**, *11* (6), 817−832.

(13) Ashkarran, A. A.; Dararatana, N.; Crespy, D.; Caracciolo, G.; Mahmoudi, M. Mapping the Heterogeneity of Protein Corona by *ex Vivo* Magnetic Levitation. *Nanoscale* **2020**, *12* (4), 2374−2383.

(14) Sharifi, S.; Caracciolo, G.; Mahmoudi, M. Biomolecular Corona Affects Controlled Release of Drug Payloads from Nanocarriers. *Trends Pharmacol. Sci.* **2020**, *41*, 641.

(15) Kittler, S.; Greulich, C.; Diendorf, J.; Koller, M.; Epple, M. Toxicity of Silver Nanoparticles Increases during Storage Because of Slow Dissolution under Release of Silver Ions. *Chem. Mater.* **2010**, *22* (16), 4548−4554.

(16) Wen, R.; Hu, L.; Qu, G.; Zhou, Q.; Jiang, G. Exposure, Tissue Biodistribution, and Biotransformation of Nanosilver. *NanoImpact* **2016**, *2*, 18−28.

(17) Yue, Y.; Behra, R.; Sigg, L.; Suter, M. J.-F.; Pillai, S.; Schirmer, K. Silver Nanoparticle-Protein Interactions in Intact Rainbow Trout Gill Cells. *Environ. Sci.: Nano* **2016**, *3* (5), 1174−1185.

(18) Liu, Z.; Escudero, A.; Carrillo-Carrion, C.; Chakraborty, I.; Zhu, D.; Gallego, M.; Parak, W. J.; Feliu, N. Biodegradation of Bi-Labeled Polymer-Coated Rare-Earth Nanoparticles in Adherent Cell Cultures. *Chem. Mater.* **2020**, *32* (1), 245−254.

(19) Bargheer, D.; Giemsa, A.; Freund, B.; Heine, M.; Waurisch, C.; Stachowski, G. M.; Hickey, S. G.; Eychmüller, A.; Heeren, J.; Nielsen, P. The Distribution and Degradation of Radiolabeled Superparamagnetic Iron Oxide Nanoparticles and Quantum Dots in Mice. *Beilstein J. Nanotechnol.* **2015**, *6* (1), 111−123.

(20) Gilbert, B.; Fakra, S. C.; Xia, T.; Pokhrel, S.; Mädler, L.; Nel, A. E. The Fate of Zno Nanoparticles Administered to Human Bronchial Epithelial Cells. *ACS Nano* **2012**, *6* (6), 4921−4930.

(21) James, S. A.; Feltis, B. N.; de Jonge, M. D.; Sridhar, M.; Kimpton, J. A.; Altissimo, M.; Mayo, S.; Zheng, C.; Hastings, A.; Howard, D. L. Quantification of Zno Nanoparticle Uptake, Distribution, and Dissolution within Individual Human Macrophages. *ACS Nano* **2013**, *7* (12), 10621−10635.

(22) Roy, S.; Liu, Z.; Sun, X.; Gharib, M.; Yan, H.; Huang, Y.; Megahed, S.; Schnabel, M.; Zhu, D.; Feliu, N. Assembly and Degradation of Inorganic Nanoparticles in Biological Environments. *Bioconjugate Chem.* **2019**, *30* (11), 2751−2762.

(23) Sangnier, A. P.; Van de Walle, A. B.; Curcio, A.; Le Borgne, R.; Motte, L.; Lalatonne, Y.; Wilhelm, C. Impact of Magnetic Nanoparticle Surface Coating on Their Long-Term Intracellular Biodegradation in Stem Cells. *Nanoscale* **2019**, *11* (35), 16488−16498.

(24) Sharma, S.; Shrivastava, N.; Rossi, F.; Thanh, N. T. K. Nanoparticles-Based Magnetic and Photo Induced Hyperthermia for Cancer Treatment. *Nano Today* **2019**, *29*, 100795.

(25) Espinosa, A.; Curcio, A.; Cabana, S.; Radtke, G.; Bugnet, M.; Kolosnjaj-Tabi, J.; Péchoux, C.; Alvarez-Lorenzo, C.; Botton, G. A.; Silva, A. K.; Abou-Hassan, A.; Wilhelm, C. Intracellular Biodegradation of Ag Nanoparticles, Storage in Ferritin, and Protection by a Au Shell for Enhanced Photothermal Therapy. *ACS Nano* **2018**, *12* (7), 6523−6535.

(26) Mazuel, F.; Espinosa, A.; Radtke, G.; Bugnet, M.; Neveu, S.; Lalatonne, Y.; Botton, G. A.; Abou-Hassan, A.; Wilhelm, C. Magneto-Thermal Metrics Can Mirror the Long-Term Intracellular Fate of Magneto-Plasmonic Nanohybrids and Reveal the Remarkable Shielding Effect of Gold. *Adv. Funct. Mater.* **2017**, *27* (9), 1605997.

(27) Zhuo, X.; Henriksen-Lacey, M.; Jimenez de Aberasturi, D.; Sánchez-Iglesias, A.; Liz-Marzán, L. M. Shielded Silver Nanorods for Bioapplications. *Chem. Mater.* **2020**, *32* (13), 5879−5889.

(28) Kreyling, W. G.; Abdelmonem, A. M.; Ali, Z.; Alves, F.; Geiser, M.; Haberl, N.; Hartmann, R.; Hirn, S.; De Aberasturi, D. J.; Kantner, K. *In Vivo* Integrity of Polymer-Coated Gold Nanoparticles. *Nat. Nanotechnol.* **2015**, *10* (7), 619−623.

(29) Goodman, A. M.; Cao, Y.; Urban, C.; Neumann, O.; Ayala-Orozco, C.; Knight, M. W.; Joshi, A.; Nordlander, P.; Halas, N. J. The Surprising *in Vivo* Instability of Near-IR-Absorbing Hollow Au-Ag Nanoshells. *ACS Nano* **2014**, *8* (4), 3222−3231.

(30) Van de Walle, A.; Kolosnjaj-Tabi, J.; Lalatonne, Y.; Wilhelm, C. Ever-Evolving Identity of Magnetic Nanoparticles within Human Cells, the Interplay of Endosomal Confinement, Degradation, Storage, and Neo-Crystallization. *Acc. Chem. Res.* **2020**, *53* (10), 2212−2224.

(31) Curcio, A.; Van de Walle, A.; Serrano, A.; Prévéral, S.; Pechoux, C.; Pignol, D.; Menguy, N.; Lefevre, C. T.; Espinosa, A.; Wilhelm, C. Transformation Cycle of Magnetosomes in Human Stem Cells: From Degradation to Biosynthesis of Magnetic Nanoparticles Anew. *ACS Nano* **2020**, *14* (2), 1406−1417.

(32) Gai, S.; Yang, G.; Yang, P.; He, F.; Lin, J.; Jin, D.; Xing, B. Recent Advances in Functional Nanomaterials for Light-Triggered Cancer Therapy. *Nano Today* **2018**, *19*, 146−187.

(33) Curcio, A.; Silva, A. K.; Cabana, S.; Espinosa, A.; Baptiste, B.; Menguy, N.; Wilhelm, C.; Abou-Hassan, A. Iron Oxide Nano-flowers@ CuS Hybrids for Cancer Tri-Therapy: Interplay of Photothermal Therapy, Magnetic Hyperthermia and Photodynamic Therapy. *Theranostics* **2019**, *9* (5), 1288.

(34) Wang, S.; Riedinger, A.; Li, H.; Fu, C.; Liu, H.; Li, L.; Liu, T.; Tan, L.; Barthel, M. J.; Pugliese, G. Plasmonic Copper Sulfide Nanocrystals Exhibiting Near-Infrared Photothermal and Photo-dynamic Therapeutic Effects. *ACS Nano* **2015**, *9* (2), 1788−1800.

(35) Marin, R.; Skripka, A.; Besteiro, L. V.; Benayas, A.; Wang, Z.; Govorov, A. O.; Canton, P.; Vetrone, F. Highly Efficient Copper Sulfide-Based Near-Infrared Photothermal Agents: Exploring the Limits of Macroscopic Heat Conversion. *Small* **2018**, *14* (49), 1803282.

(36) Li, L.; Rashidi, L. H.; Yao, M.; Ma, L.; Chen, L.; Zhang, J.; Zhang, Y.; Chen, W. CuS Nanoagents for Photodynamic and Photothermal Therapies: Phenomena and Possible Mechanisms. *Photodiagn. Photodyn. Ther.* **2017**, *19*, 5−14.

(37) Ramadan, S.; Guo, L.; Li, Y.; Yan, B.; Lu, W. Hollow Copper Sulfide Nanoparticle-Mediated Transdermal Drug Delivery. *Small* **2012**, *8* (20), 3143−3150.

(38) Chen, L.; Hu, H.; Chen, Y.; Gao, J.; Li, G. Plasmonic Cu 2- X S Nanoparticles: A Brief Introduction of Optical Properties and Applications. *Materials Advances* **2021**, *2*, 907−926.

(39) Wang, D.; Dong, H.; Li, M.; Cao, Y.; Yang, F.; Zhang, K.; Dai, W.; Wang, C.; Zhang, X. Erythrocyte-Cancer Hybrid Membrane Camouflaged Hollow Copper Sulfide Nanoparticles for Prolonged Circulation Life and Homotypic-Targeting Photothermal/Chemo-therapy of Melanoma. *ACS Nano* **2018**, *12* (6), 5241−5252.

(40) Guo, L.; Panderi, I.; Yan, D. D.; Szulak, K.; Li, Y.; Chen, Y.-T.; Ma, H.; Niesen, D. B.; Seeram, N.; Ahmed, A. A Comparative Study of Hollow Copper Sulfide Nanoparticles and Hollow Gold Nano-spheres on Degradability and Toxicity. *ACS Nano* **2013**, *7* (10), 8780−8793.

(41) Ortiz de Solorzano, I.; Prieto, M.; Mendoza, G.; Alejo, T.; Irusta, S.; Sebastian, V.; Arruebo, M. Microfluidic Synthesis and Biological Evaluation of Photothermal Biodegradable Copper Sulfide Nanoparticles. *ACS Appl. Mater. Interfaces* **2016**, *8* (33), 21545−21554.

(42) Corradini, E.; Bernardis, I.; Dongiovanni, P.; Buzzetti, E.; Caleffi, A.; Artuso, L.; Pelusi, S.; Tenedini, E.; Tagliafico, E.; Rametta, R. Rare Ceruloplasmin Variants Are Associated with Hyper-ferritinemia and Increased Hepatic Iron in Nafld Patients: Results from a Ngs Study. *J. Hepatol.* **2018**, *68*, S58−S59.

(43) Zhu, S.; Shanbhag, V.; Wang, Y.; Lee, J.; Petris, M. A Role for the Atp7a Copper Transporter in Tumorigenesis and Cisplatin Resistance. *J. Cancer* **2017**, *8* (11), 1952.

(44) Gu, J.; Xu, H.; Han, Y.; Dai, W.; Hao, W.; Wang, C.; Gu, N.; Xu, H.; Cao, J. The Internalization Pathway, Metabolic Fate and Biological Effect of Superparamagnetic Iron Oxide Nanoparticles in the Macrophage-Like Raw264. 7 Cell. *Sci. China: Life Sci.* **2011**, *54* (9), 793−805.

(45) Kurz, T.; Terman, A.; Gustafsson, B.; Brunk, U. T. Lysosomes in Iron Metabolism, Ageing and Apoptosis. *Histochem. Cell Biol.* **2008**, *129* (4), 389−406.

(46) Soenen, S. J.; Demeester, J.; De Smedt, S. C.; Braeckmans, K. Turning a Frown Upside Down: Exploiting Nanoparticle Toxicity for Anticancer Therapy. *Nano Today* **2013**, *8* (2), 121−125.

(47) Kaplan, J. H.; Maryon, E. B. How Mammalian Cells Acquire Copper: An Essential but Potentially Toxic Metal. *Biophys. J.* **2016**, *110* (1), 7−13.

(48) Liu, S.; Liu, Y.; Pan, B.; He, Y.; Li, B.; Zhou, D.; Xiao, Y.; Qiu, H.; Vijver, M. G.; Peijnenburg, W. J. The Promoted Dissolution of Copper Oxide Nanoparticles by Dissolved Humic Acid: Copper Complexation over Particle Dispersion. *Chemosphere* **2020**, *245*, 125612.

(49) Naatz, H.; Manshian, B. B.; Rios Luci, C.; Tsikourkitoudi, V.; Deligiannakis, Y.; Birkenstock, J.; Pokhrel, S.; Mädler, L.; Soenen, S. J. Model-Based Nanoengineered Pharmacokinetics of Iron-Doped Copper Oxide for Nanomedical Applications. *Angew. Chem.* **2020**, *132* (5), 1844−1852.

(50) Hugounenq, P.; Levy, M.; Alloyeau, D.; Lartigue, L.; Dubois, E.; Cabuil, V. R.; Ricolleau, C.; Roux, S. P.; Wilhelm, C.; Gazeau, F. Iron Oxide Monocrystalline Nanoflowers for Highly Efficient Magnetic Hyperthermia. *J. Phys. Chem. C* **2012**, *116* (29), 15702−15712.

(51) Ravel, B.; Newville, M. Athena, Artemis, Hephaestus: Data Analysis for X-Ray Absorption Spectroscopy Using Ifeffit. *J. Synchrotron Radiat.* **2005**, *12* (4), 537−541.



https://doi.org/10.1021/acsnano.1c00567
*ACS Nano* XXXX, XXX, XXX−XXX